Article

Integrated nano-cavity plasmon light-sources for on-chip optical interconnects

Ke Liu, Ning Li, Devendra K Sadana, and Volker J. Sorger

ACS Photonics, **Just Accepted Manuscript** • DOI: 10.1021/acsphotonics.5b00476 • Publication Date (Web): 19 Jan 2016

Integrated nano-cavity plasmon light-sources for on-chip optical interconnects

Ke Liu[†,‡], Ning Li[*,§], Devendra K. Sadana[§], Volker J. Sorger[*,†]

[†]Department of Electrical and Computer Engineering, School of Engineering and Applied Science, George Washington University, Washington, DC 20052, USA

[‡]The Key Laboratory of Optoelectronics Technology, Ministry of Education, , College of Electronic Information and Control Engineering, Beijing University of Technology, Beijing 100124, P.R. China

[§]IBM T. J. Watson Research Center, 1101 Kitchawan Road, Yorktown Heights, New York 10598, USA

ABSTRACT: Next generation on-chip light sources require high modulation bandwidth, compact footprint, and efficient power consumption. Plasmon-based sources are able to address the footprint challenge set by both the diffraction limited of light and internal laser physics such as plasmon utilization. However, the high losses, large plasmonic-momentum of these sources hinder efficient light coupling to on-chip waveguides, thus questioning their usefulness. Here we show that plasmon light sources can be useful devices; they can deliver efficient outcoupling power to on-chip waveguides, and are able to surpass modulation speeds set by gain-compression. We find that waveguide-integrated plasmon nano-cavity sources allow to transfer about ~60% of their emission into planar on-chip waveguides, while sustaining a physical small footprint of ~0.06 μm^2. These sources are able to provide output powers of tens of microwatts for microamp-low injection currents and reach milliwatts for higher pump rates. Moreover, the direct modulation bandwidth exceeds that of classical, gain compression-limited on-chip sources by more than 200%. Furthermore, these novel sources feature high power efficiencies (~1fJ/bit) enabled by both minuscule electrical capacitance and efficient internal photon utilization. Such strong light-matter-interaction devices might allow redesigning photonic circuits that only demand microwatts of signal power in the future.

KEYWORDS: *laser, nano-cavity, plasmon, photonics integration, rate equations*

For Table of Contents Use Only:

Integrated nano-cavity plasmon light-sources for on-chip optical interconnects

Ke Liu[†,‡], Ning Li*[,§], Devendra K. Sadana[§], Volker J. Sorger*[,†]

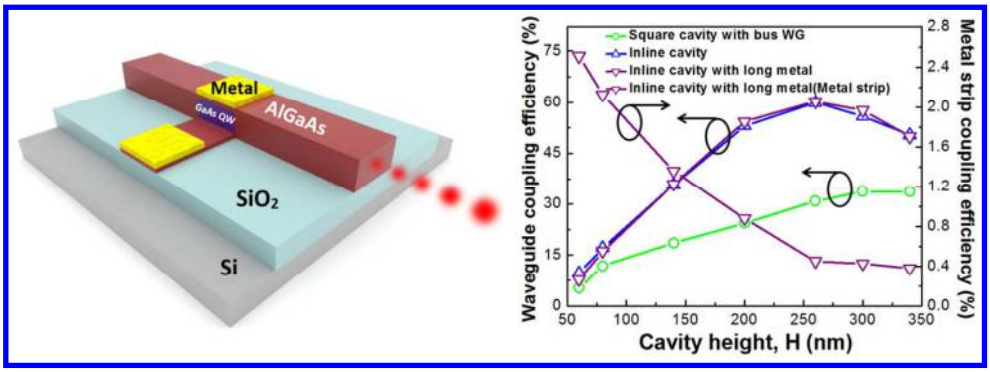

In the past decade, photonic technologies have become universal in data communications. The dense integration of photonic communication links has potential to deliver both high data throughput and bit-densities, while minimizing power consumption and energy dissipation.[1,2] In particular, solutions are needed to address both the increasing power density and data rate bottleneck between computation and communication.[3] However, the required on-chip light sources for the photonic links are challenged by 1) large footprints due to the diffraction limit of light, 2) low threshold efficiencies owing to small spontaneous emission coupling factors, β, leading to high power consumption (i.e. energy-per-bit), 3) temperature sensibilities when high-quality cavities are deployed, and 4) slow modulation speeds because of gain compression effects and parasitic electrical capacitances. As a result, network-on-chip light sources are therefore often considered off-chip.[4]

The emerging field of plasmonics, coherent electromagnetically driven electronic oscillations at metal-dielectric interfaces,[5] has demonstrated on-chip laser devices that address some of the above challenges; these include compact light sources below the diffraction limit,[6-8] operating at cryo[9,10] and room temperature,[11,12] and pulsed[13] and continuous wave operation.[14] However, these laboratory demonstrations are often unsuitable for chip integration due to a variety of limitations such as incompatibilities to telecom frequencies of the gain medium, photonic platform integration, and inability to deliver sufficient power levels into on-chip waveguides. The latter bears both fundamental and practical challenges for plasmon nanolasers in particular; the large wave vectors of sub diffraction-limited modes add profound challenges to couple the emission into a non diffraction-limited waveguide or free space efficiently. In the limit of zero-dimensional sources, the radiation pattern spreads into a 4π solid angle and bears a high source impedance of about 50 kΩ.[7] While not part of the scope of this work, we note that the latter will introduce significant losses due

to impedance mismatches when coupling to free-space is desired. In addition, practical challenges exist to efficiently utilize the emission on-chip; for instance the approach to cover the gain material with a metal to increase modal confinement blocks and absorbs emissions thus exacerbating the outcoupling challenge.[6,13-19] As such, nanolasers can often only be accessed through the device's substrate[6,20,21] or side-wall[10], thus limiting its use as source for planar circuits. While hetero-integration (i.e. III-V/Silicon wafer bonding) has demonstrated partial success,[22,23] monolithic integration is more desirable the fabrication process. However the coupling efficiency is still just about 18% for a monolithically-integrated nanoscale light-emitting diode (LED) to a plasmonic waveguide.[24] As such the design of a compact and monolithically integrated plasmon sources for efficient power delivery on-chip is still standing.

Here we investigate different plasmon source configurations for their performance and chip integration potential. Of interest is to relate the internal physical processes characterized by the cavity quality (Q) factor and the light-matter-interaction (LMI) enhancement quantified by the Purcell factor[25] to external performance values such as the achievable source output power and the 3-dB role-off modulation bandwidth as derived from the rate equations. Moreover, understanding nanofabrication-induced performance deviations are of significance and considered towards gaining a practical sense of the reliability of this class of sources. Our results show that a waveguide-embedded nanoscale plasmon source configuration delivers high coupling efficiency (~60%), a small (~0.06 μm^2) footprint enabling dense integration and a modulation potential of 100 GHz for near-lasing threshold pump rates. Relating the internal device processes to external performances (i.e. output power) we find that future on-chip sources do not have to provide milliwatts of power any more. That is, the obtainable power levels from plasmon sources as

discussed here seem to be sufficient to drive future photonic integrated circuits (PIC) that comprise of highly sensitive nanoscale opto-electronic building blocks due to low electrical capacitances, thus paving the way for a technological paradigm shift to nanoscale PICs (see discussion below).

NANOLASER PERFORMANCE

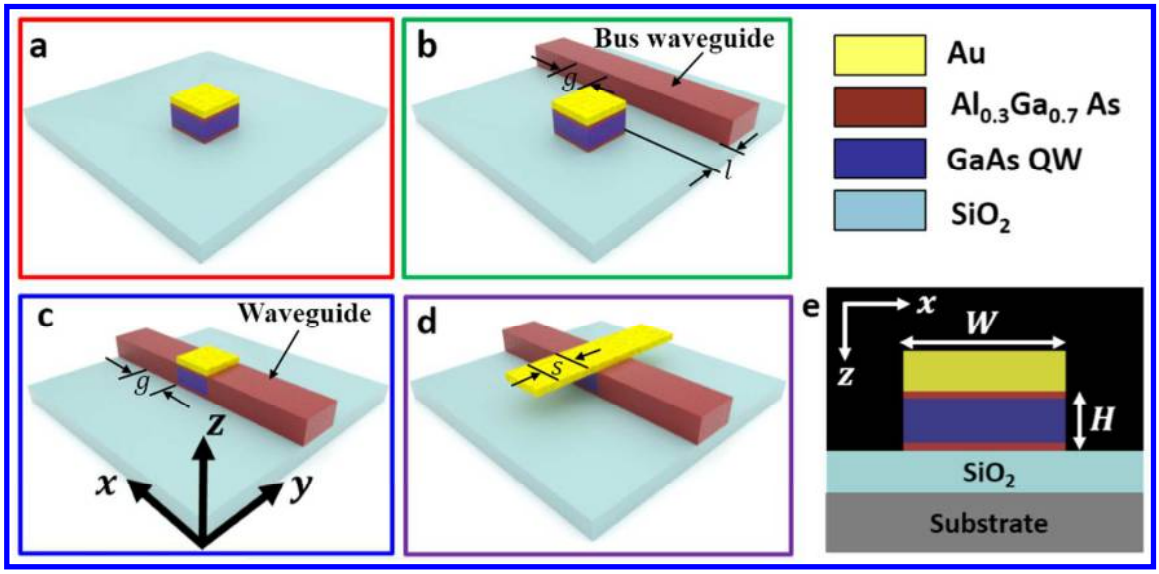

Figure 1. Three-dimensional (3D) schematic structures of plasmon-cavity based nanolasers. (a) Square cavity. (b) Square cavity with bus waveguide, l is the coupling distance between the cavity and the bus waveguide. (c) Inline cavity, g is the coupling distance away from the cavity edge along the inline waveguide. (d) Inline cavity with long metal, s is the coupling distance in the metal strip layer. The aforementioned four structures are all on a SiO_2 layer. (e) Cross-sectional view of the metal-semiconductor square plasmon resonator in the xz plane. The cavity in the z direction consists of a 20 nm $Al_{0.3}Ga_{0.7}As$ top layer, a GaAs quantum-well (QW) gain medium layer, and a 20 nm $Al_{0.3}Ga_{0.7}As$ bottom layer, where the GaAs QW gain medium involves a periodic structure with un-doped $Al_{0.3}Ga_{0.7}As$ barrier (i.e. 10 nm) and GaAs well (i.e. 7 nm) layers. The thickness of the top and bottom $Al_{0.3}Ga_{0.7}As$ layers is equal and kept constant to 20 nm each, and the total cavity height H is varied from 60 to 340 nm for the design optimization, while the Au thickness (100 nm) is unchanged for each cavity structure. The cavity size, W, is varied from 50 to 700 nm wide for determining the resonant wavelength and only the thickness of the gain material layer is varied in the simulations. The color of each rectangular frame in (a), (b), (c), and (d) represents one nanolaser cavity structure.

The optical cavity is a major component of the laser design as it encompasses the gain medium and provides feedback for the lasing mode. In order to explore and compare the nanolaser performance and usefulness, we investigated a variety of plasmon-cavity based nanolaser structures (Figure 1); (a) square cavity, (b) square cavity with bus waveguide, (c) inline cavity, and (d) inline cavity with an extended metal strip (i.e. simulating an electrical contact or via). Each cavity is formed by both the optical confinement of the dielectric loaded surface plasmon polariton waveguide,[26] and the high index contrast of the gain and cavity material relative to its surrounding. The corresponding cross-section of this cavity geometry is at the xz direction (Figure 1e). Analyzing the laser-to-waveguide coupling efficiency of these laser resonators, two waveguide coupling cases are utilized. Case one assumes a bus optical waveguide with a distance l to the square cavity (Figure 1b), whereas in case two the square cavity is inserted into a photonic waveguide forming a waveguide-integrated plasmon laser with different metal strip length (Figure 1c, d).

An initial step in the design, is to determine the resonance wavelength of the plasmon cavity since pumping the gain material require the cavity to be resonant at the wavelength within the gain bandwidth for efficient light amplification. Since the cavity's resonance wavelength scales with the cavity dimensions, we obtain a cavity width of 250 nm for the desired emission wavelength of ~850 nm, i.e. gain peak of the GaAs QW medium (Figure 2a). The fundamental transverse-magnetic (TM) (1,1,1) mode profile is indicative of providing the sub-diffraction-limited mode confinement through total internal reflection of surface plasmons at the cavity boundaries (inset Figure 2a).

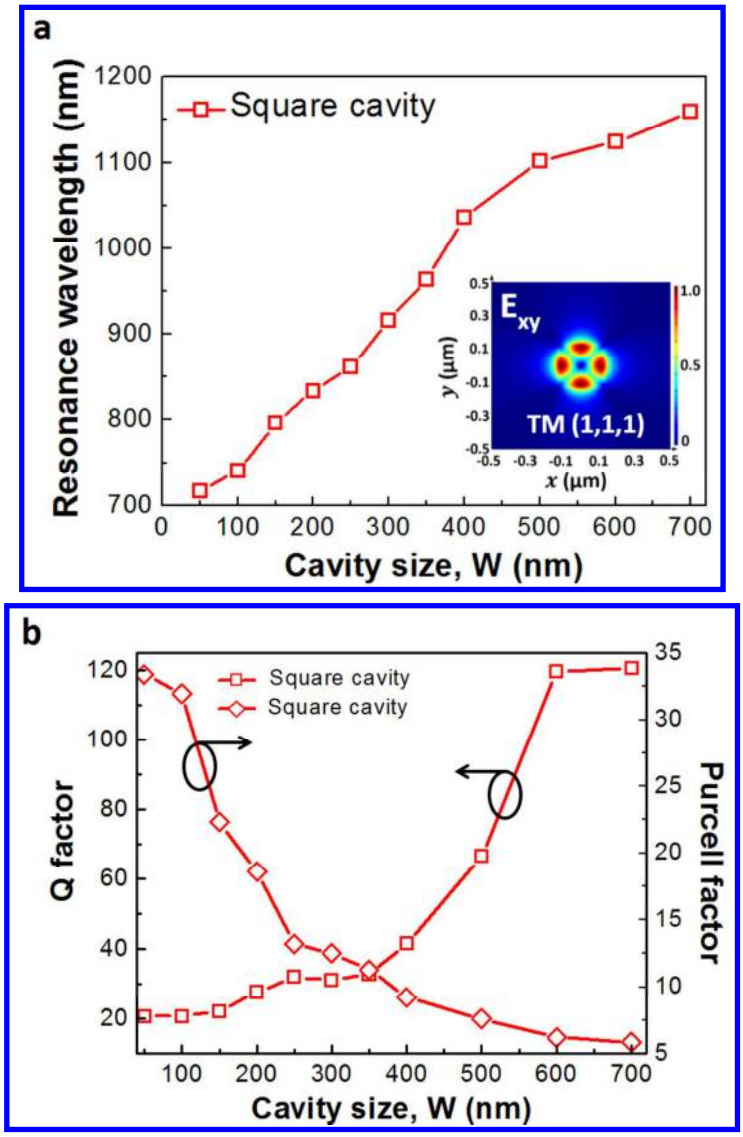

Figure 2. (a) Resonant wavelengths evolution of the square cavity with various cavity sizes (i.e. $W = 50 \sim 700$ nm), while keeping a fixed aspect ratio of 0.6 (i.e. $H/W = 0.6$). The E_{xy} plane mode is labeled as TM (p, p, q), where p and q represent the mode numbers associated with the width (W) and height (H) of the cavity, respectively.[27] The inset shows a typical fundamental TM (1, 1, 1) mode recorded in the xy plane at a distance of 20 nm away from the Au-$Al_{0.3}Ga_{0.7}As$ interface in the z-direction for the square cavity with W=250 nm. (b) Q-factor and Purcell factor dependence on the cavity size for the square cavity with a fixed aspect ratio of 0.6 (i.e. $H/W = 0.6$).

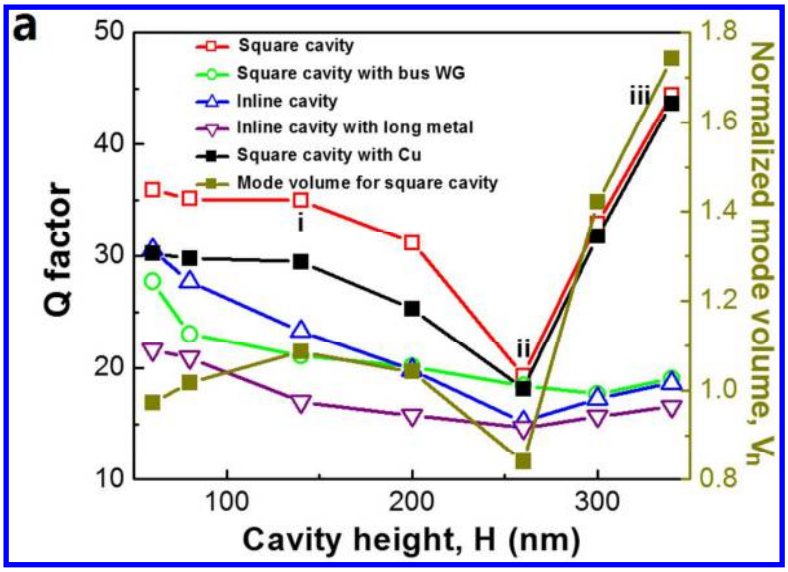
a
Square cavity
Square cavity with bus WG
Inline cavity
Inline cavity with long metal
Square cavity with Cu
Mode volume for square cavity
Q factor
Normalized mode volume, V_n
Cavity height, H (nm)
i
ii
iii

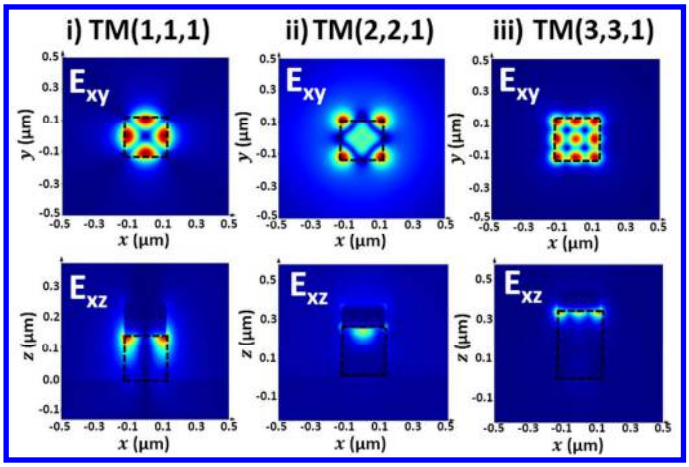
i) TM(1,1,1)
ii) TM(2,2,1)
iii) TM(3,3,1)
E_{xy}
E_{xz}
x (μm)
y (μm)
z (μm)

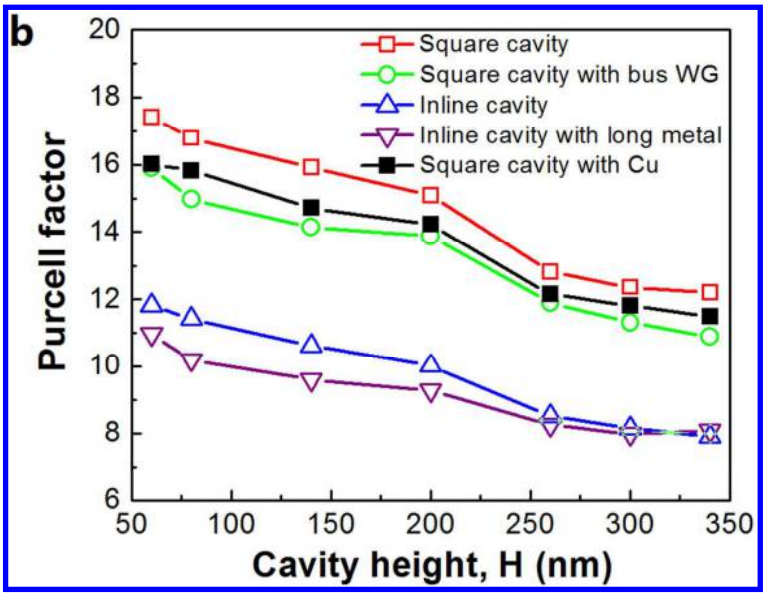
b
Square cavity
Square cavity with bus WG
Inline cavity
Inline cavity with long metal
Square cavity with Cu
Purcell factor
Cavity height, H (nm)

Figure 3. (a) Comparison of the total cavity Q factors as a function of the cavity height at a fixed cavity size of 250 nm for four plasmon nanolasers. For the case of square cavity as an example, the normalized mode volumes, V_n, are also included. The inset shows the electric field profiles of resonant modes (i.e. i, ii, iii labeled at the Q - H curve for the square cavity) in the xy plane and xz plane for the square cavity at a particular cavity height at H=140 nm, 260 nm, and 340 nm, respectively. Dashed black lines are outlining the cavity. The E_{xy} plane modes are recorded at a distance of 20 nm away from the Au-$Al_{0.3}Ga_{0.7}As$ interface in the z-direction, and the E_{xz} plane modes are recorded at the center (i.e. $y = 0$ nm) of the square cavity. (b) Comparison of the Purcell factor as a function of the cavity height, H, at a fixed cavity size of W=250 nm for the four plasmon cavities. In particular the coupling distance is zero nanometer (i.e. $l = 0$ nm) for the case of square cavity with bus waveguide (WG). The solid square lines show Q and Purcell factors for the square cavity with Cu metal atop, respectively.

Cross-referencing the evolution between the Q-factor and F_p allows generating insights with respect to the mode confinement via Equation (6) (Refer to the subsection of Resonant wavelength, quality factor, and Purcell factor in METHODS) (Figure 2b). Varying the cavity dimensions while keeping the width-to-height ratio fixed, i.e. $H/W = 0.6$, a constant Q value of ~20 is observed for a small physical size (e.g. $W = 50\sim100$ nm), which reaches 120 for larger cavities ($W = [600, 700]$ nm). However, since Q is relatively low, the strong optical confinement becomes apparent through the reasonably high Purcell factors ($F_{p\_max} = 34$). The Purcell factors' inverse trend relative to the Q factors indicates that the mode volume is expanding with increasing cavity size. In other words, the increased rate of the mode volume for each cavity size is beyond the enhancement of the corresponding of Q-factor value, which leads to a reduced F_p.

The total Q factor is generally limited by intrinsic losses (i.e. metal loss for plasmonics) and radiation losses for a plasmon cavity, thus generally low Q's are expected, and the observed values match those of similar cavity designs.[12,28] It is interesting to compare the resonant qualities of the four different device geometries from Figure 1; the square cavity shows the highest Q factors

relative to the other cavity geometry tested due to both a higher mode confinement and reduced radiative losses (Figure 3a). On the other hand, Q is inversely proportional to the radiation efficiency of the cavity, which decreases the cavity's photon density. In order to keep the intrinsic loss constant, increasing the radiation loss (i.e. reducing radiative Q-factor) can therefore lead to higher outcoupling efficiencies of a plasmon laser, and defines a trade-off between Q-factor and coupling efficiency. Towards optimizing the cavity height this trade-off Q-factor is obtained at $H =$ 260 nm (i.e. maximum power coupling) for each cavity type investigated (Figure 3a). A similar case is obtained for the coupling efficiency of a polymer-on-gold dielectric-loaded plasmonic waveguide butt-coupled to SOI photonic waveguides,[29] which also depends on the Si-Au offset distance, where the plasmonic mode need overlap with a TM SOI-waveguide mode at an optimized distance of ~300 nm for the maximized transmission efficiency. For thicker devices beyond H = 260 nm Q increases again, which can be attributed to resonant mode-switching and to a difference in the mode confinement and hence radiative loss. For example, the electric field profiles of resonant modes (i.e. E_{xy} and E_{xz}) for the square cavity change its modal shape clearly when the resonance switches from a TM (1,1,1) to a TM (2,2,1) mode. For the latter, the profile displays the fundamental corner-bound mode, which is quite lossy ((ii) Figure 3a), whereas the TM (3,3,1) is a higher order mode with a larger modal profile and higher Q ((iii) Figure 3a).

Towards verifying the existence of a plasmonic cavity mode, we compare the group index of the laser with a photonic control design. In detail we test the fundamental cavity modes and further investigate the sensitivity to geometrical parameters such as cavity height. A range of group indices between 7.5 and 6.6 is observed at each corresponding resonant wavelength from H=60 nm to 340 nm, which may be considered as the independency of height versus width for our cavity. The

average group index for these plasmonic modes is about 7.0, which is higher than that of a photonic mode for the same cavity (without any metal) resulting in a group index of about 3.7. While higher group indices were observed for previous plasmon lasers, the results here suggest a plasmonic mode character.

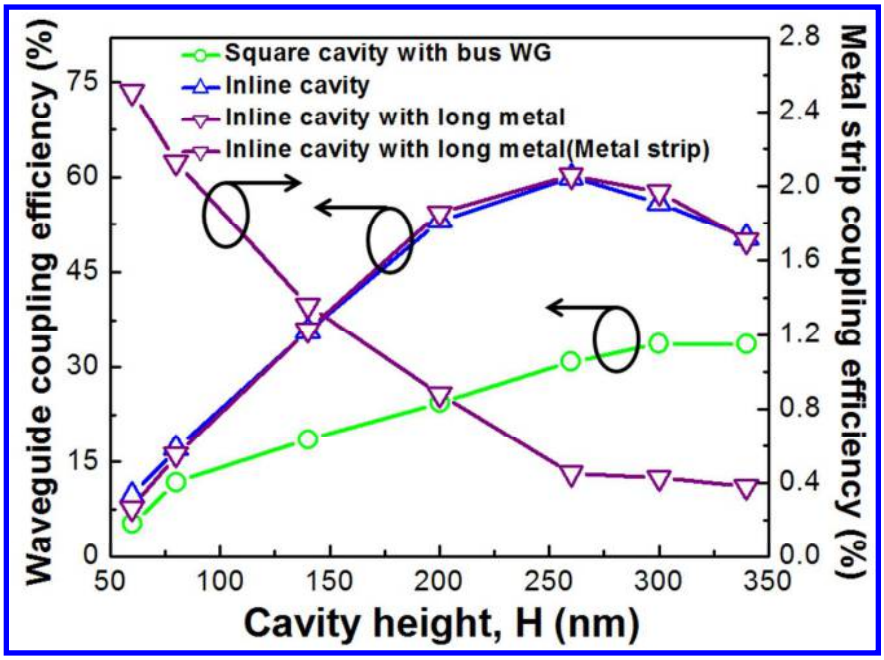

Figure 4. Comparison of coupling efficiency for four-nanolaser plasmon cavities to the neighboring $Al_{0.3}Ga_{0.7}As$ waveguides as a function of the cavity height as W = 250 nm for the square cavity with bus waveguide, inline cavity, and inline cavity with long metal. For the case of inline cavity with long metal, the coupling efficiency to the metal strip atop is also included. The coupling powers are recorded on both sides along the waveguide by power monitors, at $l = 0$ nm for the square cavity with bus waveguide, $g = 250$ nm for the inline cavity and inline cavity with long metal, respectively, and $s = 250$ nm for the metal strip of the inline cavity with long metal.

The Purcell factor exhibits a descending trend with cavity height for the four cavity cases (Figure 3b, see supporting information). Here, the square cavity exhibits the highest F_p, which can be understood by the highest optical confinement due to the strongest index difference between the

cavity and its surroundings. Note, comparable F_p values are observed for nanowire-based plasmon lasers before.[8] For the inline cavity Equation (6) (Refer to the subsection of Resonant wavelength, quality factor, and Purcell factor in METHODS) predicts V_n to be ~0.9 $(\lambda/2n_{cav})^3$ at the cavity height of $H = 260$ nm, just a sub diffraction-limited mode. The importance of the mode volume is that it affects the light intensity inside the resonator, and therefore determines the LMI strength. Rather than to extract V_n from Equation (6), we directly calculate the normalized mode volumes for the square plasmonic cavity using Lumerical FDTD Solutions (Figure 3a). The mode volumes are close to sub diffraction-limited modes for the thinner devices within H = 260 nm, and the larger mode volumes of the devices beyond H = 260 nm are due to the resonant mode-switching.

To date Gold or Silver are the preferred materials used in plasmonics due to their relatively low ohmic loss (i.e. low extinction coefficient) at visible and near infrared frequencies. However, both metals are not compatible with the CMOS technology limiting the production options of the laser. In order to allow for a CMOS option we also investigate the performance of Q and Purcell factor for Copper (Cu) as a plasmonic pad. We find a drop of Q (F_p) of about 15% (10%) to be relatively modest (Figure 3a, b). This positive result can be attributed to the extinction coefficient (i.e. κ) of Cu being higher than that of Au at the laser design frequency (~850 nm) leading to slightly larger intrinsic loss in the cavity. Coupling light efficiently out of the device and into a neighboring photonic waveguide is particularly challenging for a plasmon source with a diffraction-limited mode size due to the impedance mismatch between the sources and the on-chip waveguide. For the inline cavity case discussed here, a maximum coupling efficiency of ~60% can be obtained for both cases of the inline cavity and inline cavity with the long metal (Figure 4). Here the waveguide (or metal strip) coupling efficiency is defined by the ratio of the total power coupled

to a waveguide (i.e. cavity mode power to a waveguide) and the total radiated power from the cavity.[21] A sensitivity analysis on the coupling efficiency with respect to the laser-to-waveguide coupling distance, g, for the inline cavity shows a relatively constant coupling efficiency of ~60% (see supporting information). This indicates that the plasmonic mode excited by a dipole source in the cavity successfully converts to propagating waveguide modes. The coupling efficiency as a function of laser height (Figure 4) exhibits a maximum, and scales inversely to the Q-factor (i.e. Figure 3a). With optical interconnect applications in mind the goal is to couple the emission into a low-loss, photonic waveguide on-chip, and not utilize the emission in a plasmonic strip where propagation lengths are limited to just tens of micrometers. In this regard, we test the inline cavity's capability to enable the emission to pass into the butt-coupled photonic waveguide. Here, we extended the long metal strip above the active gain region as to allow surface plasmons coupling, which simulates a biasing contact (Figure 1d). Indeed the inline cavity only loses 1-2% of the emission into this plasmonic strip. This is significantly lower compared to designs with very thin dielectrics.[30] We note that when the square cavity is touching the waveguide ($l = 0$ nm) the maximum coupling efficiency is only about half of that of the inline case. A possible reason for this low coupling efficiency might be related to the sharp (90^o) angle, where the emission enters the waveguide, which leads to back reflection. A waveguide side-wall grating to facilitate coupling might be a solution if this case is desired. Furthermore, the coupling from the plasmonic square cavity to the photonic waveguide does not behave like a scaled-down version of an optical fiber coupling to a high-Q ring;[31] the power transfer declines monotonically with wider distance, l, and no critical, under, nor over coupling phenomenon is observed, which could be due to the localized, sub-wavelength nature of the cavity mode. Furthermore, we monitored the radiated power from the

bottom of the square cavity, since metal capped or cladded cavities have been found to often emit into the substrate (see supporting information). The results show that a maximum power coupling of about a quarter can be achieved using this method due to the cavity mode (E_{xz} field) tightly confined at the interface between metal and dielectric (inset Figure 3a).

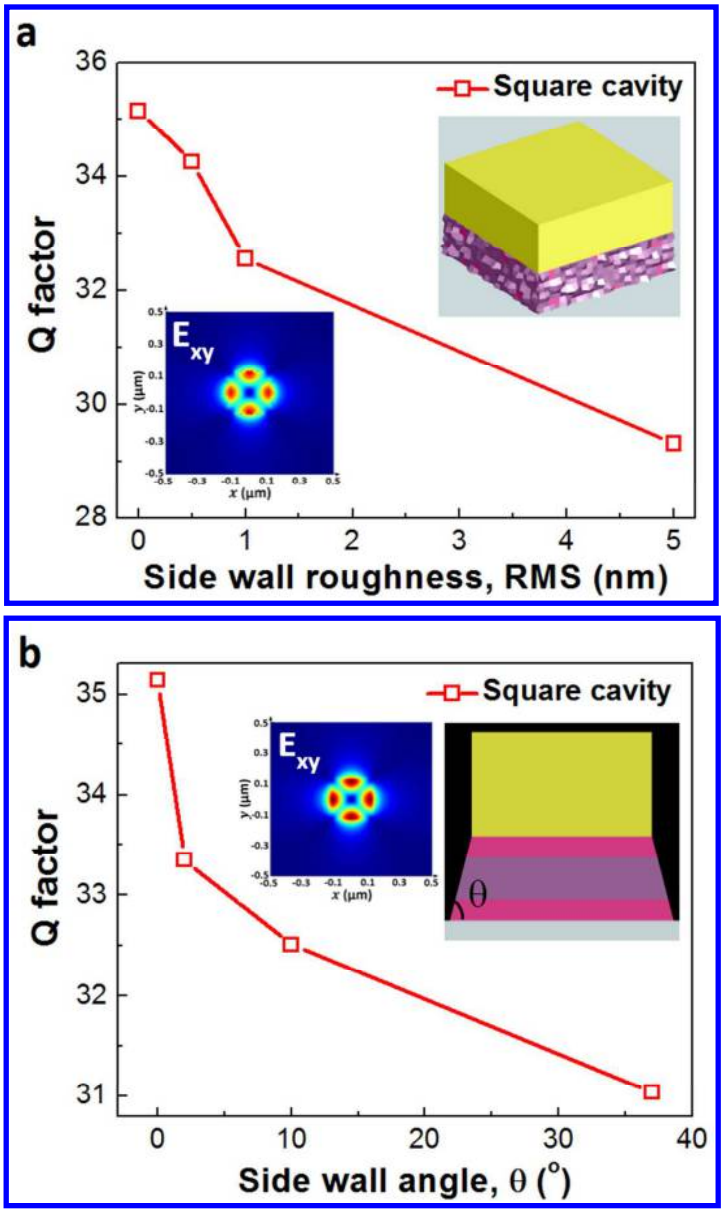

Figure 5. Total cavity Q factors dependence on (a) Side-wall roughness with root mean square (RMS) values, and (b) Side-wall angles, for the square cavity. The cavity height, 80 nm, is fixed as an example. The TM (1,1,1) modes at the cavity with 5 nm RMS roughness and with 37° side-wall angle are recorded at a distance of 20 nm away from the

Au-$Al_{0.3}Ga_{0.7}As$ interface in the z-direction, respectively. The other inset for each figure shows the schematic of the device covered with rough side-wall and with tilted side-wall, respectively. Surface roughness is added from the "Surface" category in the structure group of Lumerical finite-difference-time-domain (FDTD) software.

Nano-fabrication processing can be a major challenge for the realization of nano-laser devices. A MQW GaAs wafer is transferred to SiO_2/Si substrate first through a conventional molecular bonding technique,[32] and then followed by the fabrication of the device. Precise fabrication steps are usually needed to minimize extra cavity losses, including scattering due to surface roughness and radiative loss due to tilted side-walls.[33] We tested the nanolasers of this work in relation to the both loss factors (Figure 5). We find that the total cavity Q-factor is relatively stable (ΔQ~10%) to both roughness (1-5 nm route-mean-square, a typical range of surface roughness for GaAs with plasma etching) and non-vertical sides walls (up to 37 degrees displacement) (Figure 5b). The reason for both cases are linked to the tight optical confinement; that is most of the electric field is well concentrated within the cavity and not much field reaches the side-wall (inset Figure 5a). In addition, the field confined around the interface between the metal and the dielectric (inset Figure 5b) is not much related to the side-wall angles. Such stable design criteria for plasmon lasers are promising indicators for device integration into on-chip networks.

OUTPUT POWER AND MODULATION BANDWIDTH

Plasmon nanolasers may operate at elevated cavity losses because of their high spontaneous emission factor, β, compared to a conventional diffraction-limited laser. A high β results from the increased LMI strength, accelerating both spontaneous and stimulated emission rates beyond those available to emitters in diffraction-limited cavities. This opens the possibility to achieve lasing action of plasmons with realistic pump rates despite high cavity losses.[34] Here β is defined by the ratio of

the spontaneous emission rate into the lasing modes and the spontaneous emission rate into all the modes, and can be calculated via,[35]

$$\beta = \frac{F_{cav}^{(1)}}{\sum_k F_{cav}^{(k)}} \quad (1)$$

where the lasing mode is indicated by the index $k = 1$, and the summation is over all the modes k, including the cavity modes and the modes radiating out of the cavity into free space. To compute the β-factor, the total spontaneous emission rates into all the modes is calculated by the averaged Purcell factor using a vertically z-oriented electric dipole excitation source placed in a random position in the cavity, whereas the spontaneous emission rate into the lasing mode is evaluated by the Purcell factor using the same electric dipole excitation source purposely located the position where a cavity lasing mode exist (i.e. a highest Q value for the mode).

Towards achieving a theoretical understanding of the nanolaser characteristics through the Purcell effect, the steady state rate equations are adopted for a sub-wavelength mode volume laser device under continuous pumping,[34]

$$\frac{dn}{dt} = P - An - \beta\Gamma AS(n - n_0) - (v_s S_a / V_a)n \quad (2)$$

$$\frac{dS}{dt} = \beta An + \beta\Gamma AS(n - n_0) - \gamma S \quad (3)$$

where P is the pump rate, S is the photon number of a single lasing mode, n is the excited state population density, A is the spontaneous emission rate, which can be modified by the Purcell effect via $A = F_p A_o$, where A_o is the natural spontaneous emission rate of the material, and $A_o = 1/\tau_{sp0}, \tau_{sp0}$ is the spontaneous emission lifetime of gain medium. Γ quantifies the overlap between the spatial distribution of gain medium relative to a lasing mode, and is about 50% for the square cavity case as evaluated by calculating the spatial-overlap of the cavity mode profile with the physical dimensions of the GaAs QW region. S_a and V_a are the exposed surface area (i.e. side

walls of the nanolaser) and the gain material's volume, respectively. v_s is the surface recombination velocity, and here v_s=4500 cm/s is used for GaAs surface passivation using an oxide deposition method.[36] n_0 is the excited state population at transparency, γ is the total cavity loss rate per unit volume (i.e. total loss coefficient per unit length × modal speed/V_{mode}), and $\gamma = \gamma_c + \gamma_g$, where γ_c is the loss rate due to cavity mirror loss and intrinsic loss, and γ_g is the absorption loss rate due to the gain medium that is related to the GaAs absorption coefficient, i.e. ~9.0×10^3 cm^{-1}.[37] In order to relate the rate equations to the power output, P_{out}, can be written as,[38]

$$P_{out} = \eta_c \frac{\alpha_m}{\alpha_m+\alpha_i} \frac{S_{ph}}{\tau_p} \frac{hc}{\lambda} V_{mode} \quad (4)$$

where η_c is the collection efficiency representing the ratio of the coupling power to the total radiated power (i.e. waveguide coupling efficiency in Figure 4), α_i (α_m) is the cavity intrinsic (mirror) losses per unit length, i.e. 1.7×10^3 cm^{-1} (2.1×10^3 cm^{-1}) for the inline cavity, 2.4×10^3 cm^{-1} (1.5×10^3 cm^{-1}) for the inline cavity with long metal, and 1.8×10^3 cm^{-1} (1.3×10^3 cm^{-1}) for the square cavity with bus waveguide, respectively. S_{ph} is the photon density, τ_p is the photon life time, and is proportional to the cavity Q (i.e. $\tau_p = Q/(2\pi f)$, f is the cavity resonant frequency), h the Planck constant, c is the light speed in vacuum, and λ is the lasing wavelength.

The inline cavity laser with a β-factor of ~0.55 exhibits the highest output power compared to the other two structures (Figure 6a), which approaches 80 μW at threshold (i.e. $P/P_{th} = 1$) and even 1 mW at $P/P_{th} = 10$, respectively, where P_{th} is the threshold pump rate, and $P_{th} = [\gamma_c(A + v_s S_a/V_a) + \gamma_g((1-\beta)A + v_s S_a/V_a)]/\beta\Gamma A$. However, the injection current density at the threshold pump rate is calculated to be ~3×10^3 kA/cm^2 for a $W = 250$ nm size cavity. In practice the high power output at the high current density might have to operate with a proper thermal management design, and similar order of magnitude threshold pump intensity is observed for the

nanowire plasmon lasers.[9] When pumping far below the threshold pump at room temperature, these plasmon nanolasers behave as an amplified spontaneous emission light source. For instance, an output power of 20 μW corresponds to an acceptable injection current of ~800 μA for the inline cavity, where the device operates as a nano-cavity LED source (Figure 6b).

The inline cavity laser features a sub diffraction-limited mode volume, which significantly increases β-factor by 2-4 orders of magnitude compared to a conventional laser (i.e. β=10^{-5}~10^{-3}). This subsequently reduces the threshold pump rate and increases the photon utilization thus providing a higher relative output power. In addition, the photon density represents the extent of LMI, and is directly proportional to the output power of the laser, and is estimated to be in the range of 10^{16}-10^{17} cm^{-3} for this laser device, which is 1-2 orders higher than a conventional diffraction-limited laser (e.g. ~10^{14}-10^{15} cm^{-3}).[39]

Another important measure for the performance of plasmon nanolasers is the modulation bandwidth (i.e. 3-dB role-off speed). Here we estimate the small signal response of the plasmon laser by observing the spectral response function,[40]

$$H(\omega) = \frac{\beta\Gamma_T(1+S_0)}{\sqrt{(\omega^2-\omega_r^2)^2+\omega^2\omega_p^2}} \quad (5)$$

where ω is the optical cavity angular frequency, Γ_T is the transition rate of excited state population, which is equal to the spontaneous emission rate, A. $\omega_p = \gamma_c + \Gamma_T(1-\beta N_0+\beta S_0)$, and $\omega_r^2 = \Gamma_T[\gamma_c(1+\beta S_0)-\beta(1-\beta)\Gamma_T N_0]$, S_0 and N_0 are the steady-state photon number and population inversion number, respectively, and $\gamma_c = 1/\tau_p$, The time response of a nanolaser is characterized by the modulation bandwidth, f_{3dB}, defined as the frequency at which the response function decays to half of its zero-frequency value (i.e. $H(\omega)/H(0)$). When the nanolaser device is operated below the threshold current (i.e. ~2 mA calculated for our case), it effectively operates as a nano-cavity LED.

The frequency response of the device below lasing threshold is calculated using the spontaneous emission lifetime, which is equal to carrier lifetime but neglecting the non-radiative recombination lifetime. In this type of nano-cavity LED, the spontaneous emission lifetime is inversely proportional to the Purcell factor. As a result the nano-cavity LED can operate at a much higher modulation speed than a conventional LED. For example, the modulation frequency of the inline cavity LED increases with the pump rate (Figure 6c) resulting in a 3-dB bandwidth of more than 40 (80) GHz at a 0.5 (1.0) of the threshold pump rate.

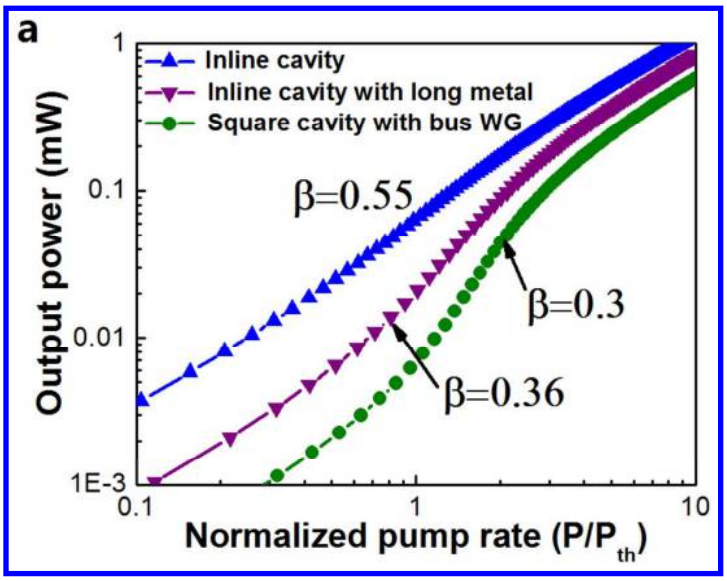

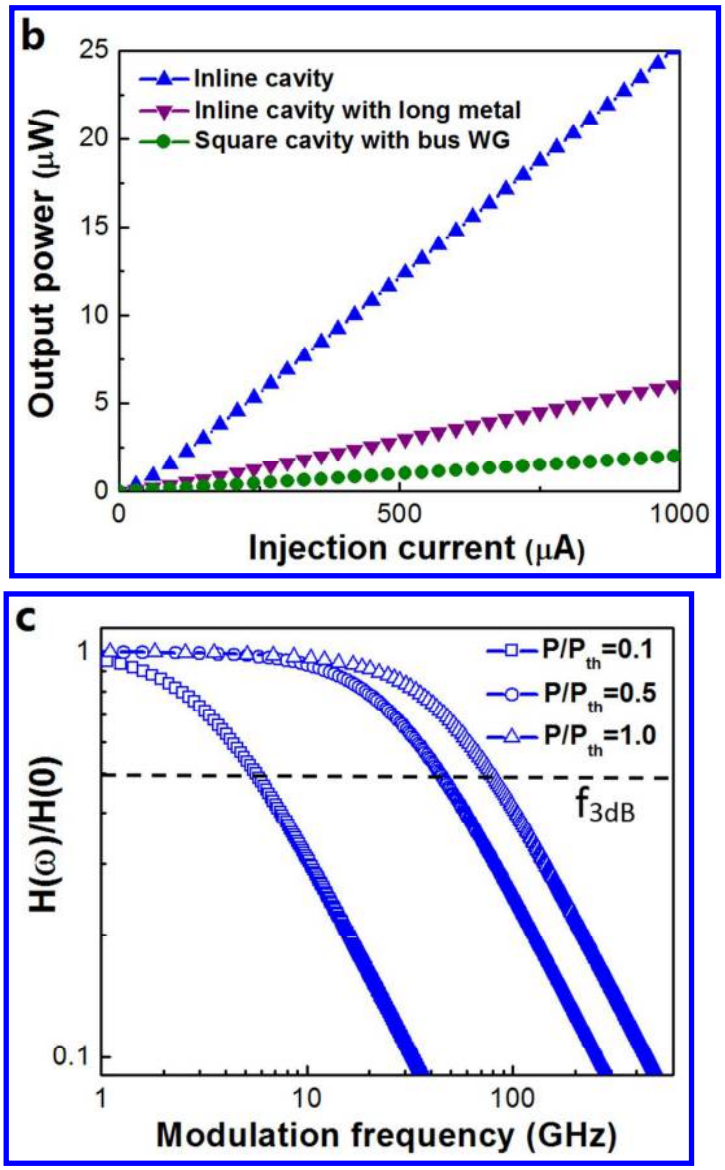

Figure 6. (a) Laser output power as a function of normalized pump rate (i.e. P/P_{th}) for the three plasmon nanolasers. The corresponding β factors calculated for each structure are also shown. (b) Practical light output power dependence on the injection current for the various plasmon nanolasers. (c) Modulation bandwidth of the inline cavity nanolaser/LED at the different pump rates with below and equal threshold pump rate. A ~80 GHz modulation frequency is calculated at a 3 dB bandwidth with the pump rate of $P/P_{th} = 1.0$.

LASER INTEGRATION

For an electrically-pumped nanolaser, self-heating may lead to temperature instabilities in the

semiconductor due to joule heating of the small device volume. A proper design for improving the temperature distribution in nanolasers[41] is an important aspect particularly when device bonding on a Silicon-on-insulator (SOI) platform is considered since the thermal conductivity of Silica is about two orders of magnitude lower compared to a bulk Silicon substrate, thus contributing to heat dissipation lockage. Therefore we investigate the ability of the inline cavity nanolaser to operate below CMOS temperature budgets (<350 K), and consider an electrically-pumped device (Figure 7a) analyzing the temperature profile (Figure 7b, c). Here the plasmon cavity metal pad (i.e. Cu) synergistically serves as an electrical contact, and we hypothesize that is also acts as a dissipative heat sink. Our results show that this nanolaser is able to operate at ~65^{o}C at pump threshold (~2000 μA), which is about 15^{o}C below of the operation temperature of a typical CMOS integrated circuit. It is intriguing to ask whether the plasmonic metal provides for a better heat sink than a low-resistive dielectric. In order to test this, we replaced the metal cavity/contact with highly doped poly-Silicon (see supporting information), and repeated the experiment. The resulting heat maps indicate a maximum device temperature increase to ~95^{o}C at threshold, thus highlighting the importance of the metal pad towards realizing nanoscale laser that are able to adhere to thermal budgets. Such thermal management solution using passive and synergistic designs are important to ensuring temperature stability of nanoscale devices without adding footprint, additional material or process overhead. These results are encouraging and future research should map out the limits of this technological option. Another desired yet challenging task is to integrate optical components monolithically on-chip. Here new circuit design opportunities can be envisioned enabled by hetero integration of active nanoscale III-V-based devices into Silicon CMOS. A successful implementation can increase the degree of freedom in an interconnect design architecture, and might reduce processing cost while

maintaining a high density of interconnects, which potentially improves the performance of the optical link and network-on-chip architectures. Current nanolaser designs can be integrated onto a SOI platform through the latest III-V-to-Si wafer bonding solutions.[22]

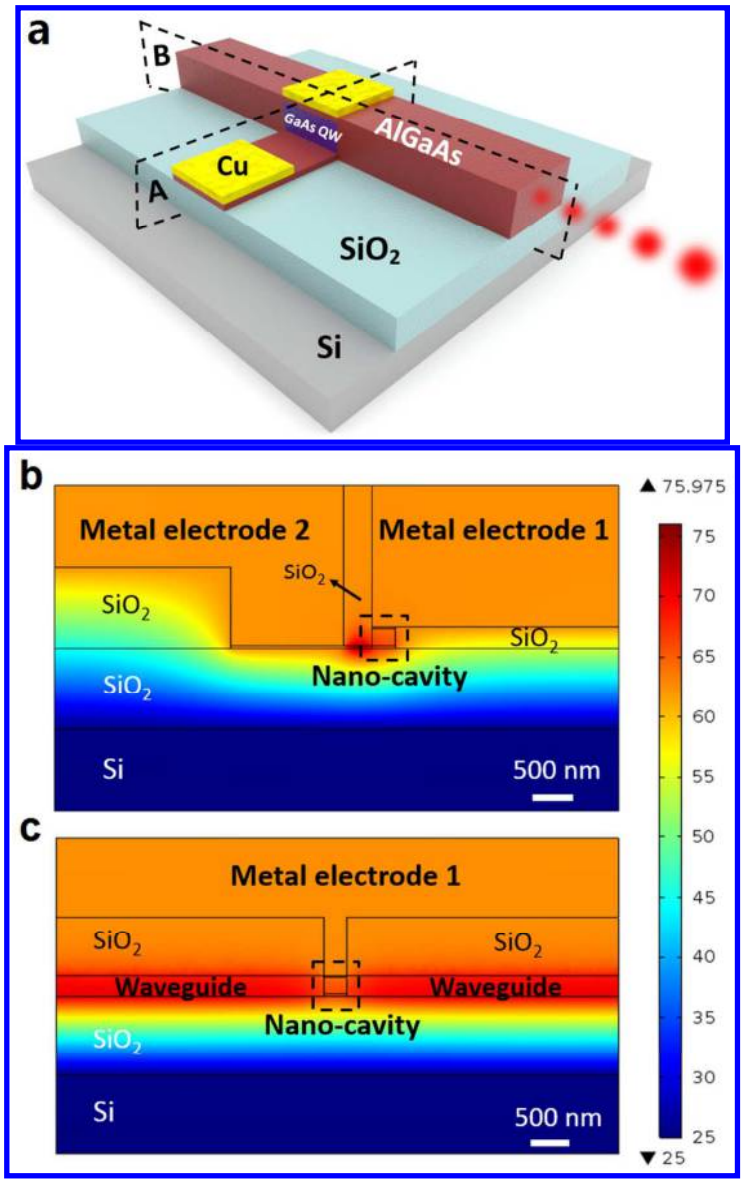

Figure 7. (a) Schematic of an electric-pumping scheme for the inline cavity nanolaser bonded on a SiO_2/Si substrate. Here Copper is used for the metal electrodes to ensure CMOS compatibility. Surface temperature distribution profiles at threshold ($P_{pump} = I_{th} =$ 2000 μA) at the (b) A plane and the (c) B plane, respectively. The results indicate a temperature of about 65°C for the laser cavity, leaving 15° of thermal budget to typical CMOS limits (80°C). Thermal conductivity (in W/m·K) of each material at room temperature: k_{Cu} = 400, k_{SiO2} = 1.38 , $k_{Si\text{-}intrinsic}$ = 130, and $k_{Si\text{-}poly}$ = 45).

With the possibilities for on-chip sub-wavelength-scale laser sources the question of viability and utilization must be raised. Here, we briefly discuss the electrical power consumption as a function of the devices' power efficiency (i.e. energy per bit), operating data-rate (i.e. in Gbps), and power dissipation density (i.e. in W/cm^2) of these novel sources in the context of next generation PICs. From the power efficiency of the source the average number of photons per bit defines three technological regimes (Table 1); diffraction limited devices have a relatively high power consumption prohibiting scaling beyond ten's of devices on-chip. This effect is well known since PIC designers usually demand 10's of milliwatts of optical power per wavelength channel. However if active optoelectronic components are miniaturized into the nanoscale regime, their wall-plug power consumption should decrease from being capacitive limited (i.e. E/bit = $\frac{1}{2}CV^2$,[42] where C is the device capacitance, and V is the driving voltage), to device intrinsically limited (i.e. carrier lifetime, cavity response function etc), if the same drive voltage can be used. This also leads to an increased operational bandwidth of the device due to a lower RC delay time, provided the device and contact resistance can be kept low. For the nanolasers for instance, the direct modulation speed also increases due to the Purcell effect. Thus, at reasonably low data rates (i.e. 10 Gbps) just ten's of micro-watts of power per device are required making the case for the nano regime to be the next generation building blocks for on-chip networks, and integrating thousands of photonic devices on-chip. The quantum regime would be the next-technology regime, where only a few photons per bit are needed. The requirements for the nano and quantum regime, however, are very strong LMI enhancements, which can be quantified by a factor proportional to Q/V_n. This optical concentration factor can be derived from Fermi's Golden Rule, resulting in two fundamental options to enhance the LMI's; (a) through strengthening the optical field intensity at the emitter, or (b) by increasing the

number of available optical modes to radiate into.[38] While the former relates to increasing the optical confinement (e.g. surpassing the diffraction limit as demonstrated in plasmonics or slot-waveguides), the latter relates to the optical density of states (DOS) per unit frequency (e.g. cavities, or emission selection rules). Starting from Fermi's Golden Rule we can thus write the interaction rate as $\gamma_{interaction} = |E(\vec{r})|^{k}_{emitter} \times DOS(\omega)$, where E is the electric field at the emitter location, and *DOS* depends on the dimensionality of the optical system, and k is an optical effect-order integer. Physically speaking, this means that one can enhance the LMIs by optically storing energy inside the cavity (i.e. $Q=\omega/\gamma_e$, where γ_e is the cavity loss rate) or by reducing the optical mode volume beyond the diffraction limit of light, which increases the modal electric field. The latter places a fundamental boundary for classical photonics devices due to diffraction-limited modes. These limitations become profound in the modulation performance of lasers and LEDs as discussed here, but also in electro-optic modulators.[43] However, the ultimate PIC scaling might not actually depend on the source, but on the receiver sensitivity, which is limited by shot- and Johnson noise. However, for plasmonic-based nanoscale photodetectors the area and capacitance can be reduced on the basis of enhanced light absorption.[44] Their scaled-down capacitance demands a greatly reduced optical power input to provide the same photodetector output voltage.

CONCLUSION

In conclusion, we investigated monolithically integrated plasmon nano-cavity-based lasers as viable light sources on-chip utilizing III-V gain materials. Our results show that more than ~60% of the laser emission can be coupled into neighboring on-chip waveguides. This contrasts metal clad or square cavities whose the waveguide collection efficiency is as low as ~24%. Furthermore, such

nanoscale cavities allow for dense integration due to the optical mode caused by dielectric loaded surface plasmon polaritons confinement to sub-diffraction limited mode volume with ~0.9 $(\lambda/2n_{cav})^3$. This increases the light-matter-interaction rate of the emitter leading to preferred emission channels and high spontaneous emission coupling factors exceeding 0.5. These light sources produce about 20 μW of optical power for medium injection currents of about 800 μA, and are able to be faster modulated than gain compression-limited devices due to the Purcell effect of strong light-matter-interaction with 3dB role-off frequencies exceeding 80 GHz at threshold. In addition to the high performance, seamless PIC integration, these lasers are benign with temperate and fabrication process constrains such as monolithic growth on III-V substrates or bonding to SOI platforms. Furthermore, we show that the plasmonic metal pad also helps to cool the laser by about 30 degrees. With such new on-chip sources, it is interesting to note, that future communication links might only require microwatts of optical power due to the fundamental limits set by new efficiency standards determined by both the optical modal confinement and the device as shown here. This next technological step is important since inefficiencies of current diffraction-limited photonics appear prohibitive to enable dense photonic integration densities. As such, the presented sources might facilitate integrating thousands of photonics devices on-chip.

METHODS

Cavity model. The design analysis is performed using commercially available 3D FDTD software (Lumerical Solutions, Inc.). The input of complex refractive indices (i.e. n and κ) of Gold, GaAs, and SiO_2 are taken from the solver's built-in material database. For the alloys of the utilized III-V material ($Al_xGa_{1-x}As$) data from reference 45 is used for the dispersion relation according to the

Kramers-Kronig relations, where an analytic fitting function (multi-coefficient material model, termed by 'FDTD model') generates the required index data in the bandwidth of interest (0.75 - 1.0 μm). Optically the dispersion of quantum wells versus bulk for the gain material GaAs/AlGaAs are rather close and show a maximum difference of about 0.04 at the cavity wavelengths.[46] In order to provide a plasmon excitation, a vertically oriented (i.e. z-direction) electric dipole source is placed inside each cavity to excite the cavity resonance. Key to excite the cavity's resonance homogeneously, which is achieved by placing a dipole source closely to the cavity edge (i.e. $W/8$) in the xy plane 20 nm away from the Gold-semiconductor interface. This ensures exciting the TM-polarized cavity modes.

Resonant wavelength, quality factor, and Purcell factor. The Q-factor being a measure of the time electromagnetic energy stored inside a cavity is influenced by both the optical feedback mechanism (e.g. mirror reflectivity) and the internal loss, and varies for different modes. The lasing mode that lies perpendicular to the cavity's boundary surfaces forms a standing-wave pattern (inset Figure 3a). Here, the Q-factor is calculated from the Fourier transform of the electromagnetic field by finding the resonance frequencies (f_R) of the signal and measuring the full width at half maximum (Δf) of the resonant peaks Δf, i.e. $Q = f_R/\Delta f$. A Q-factor analysis of the solver is utilized and determining the corresponding resonant wavelength (i.e. f_R) for each resonant mode. The cavity mode with the maximum Q value is used to determine the cavity's resonant wavelength, since it bears the highest potential to overcome the cavity losses first.

As indicated above, the Purcell factor indicates the interaction strength between photons in the cavity and the laser gain medium by quantifying the spontaneous emission rate enhancement of an

emitter inside a cavity. The dipole excitation source deployed allows for direct visualization of the Purcell factor, F_p, where the procedure is equivalent to dividing the power emitted by a dipole source in the cavity environment by that of a homogeneous bulk material.[47] A formula widely used for the evaluation of F_p is given by,[25]

$$F_p = \frac{6}{\pi^2}\left(\frac{Q}{V_n}\right) \quad (6)$$

where V_n is V_{mode} normalized to $(\lambda/2n_{cav})^3$(i.e. typically referred to as the diffraction-limited volume in a cubic half-wavelength in material), i.e. $V_n = V_{mode}/[(\lambda/2n_{cav})^3]$, λ is the resonant free space wavelength of the cavity, and n_{cav} is the cavity material index. V_{mode} is the effective mode volume, which is estimated from a commonly used definition, $V_{mode} = \frac{\int \varepsilon|E(r)|^2 dV}{\max[\varepsilon|E(r)|^2]}$, through Lumerical FDTD Solutions, where ε is the dielectric constant, $E(r)$ is the electric field strength, and V is a quantization volume encompassing the resonator and with a boundary in the radiation zone of the cavity. Equation (6) states F_p to be proportional to the ratio of the cavity's Q-factor divided by the normalized mode volume. If the cavity lineshape is much wider than the gain medium inhomogeneous broadening lineshape, Equation (6) is valid.[35] Otherwise, F_p follows the trend of mode volume with a negligible effect of cavity Q factor. For our low Q plasmonic cavity, the aforementioned case exists, and Equation (6) can be used.

AUTHOR INFORMATION

Corresponding Authors

* E-mail: sorger@gwu.edu (VS); lini@us.ibm.com (NL)

Notes

The authors declare no competing financial interest.

ASSOCIATED CONTENT

Supporting Information. Description of simulation method for Purcell factor; Determination of cavity losses; Bottom coupling efficiency of the square cavity nanolaser; Modulation bandwidth at the above threshold for the inline cavity nanolaser; Dimensions and material properties used for thermal analysis of an inline cavity laser. This material is available free of charge via the Internet at http://pubs.acs.org.

ACKNOWLEDGMENTS

VS and KL acknowledge support from the Air Force Office of Scientific Research (AFOSR) under the award numbers FA9559-14-1-0215 and FA9559-14-1-0378. NL and DKS thank Jean-Oliver Plouchart, Tak Ning, and Effendi Leobandung from IBM Research for helpful discussions.

REFERENCES

1. Shacham, A.; Bergman, K.; Carloni, L.P. Photonic networks-on-chip for future generations of chip multiprocessors. *IEEE Trans. Comput.* **2008**, 57, 1246-1260.
2. Heck, M.J.R.; Chen, H.W.; Fang, A.W.; Koch, B.R.; Liang, D.; Park, H.; Sysak, M.N.; Bowers, J.E. Hybrid Silicon photonics for optical interconnects. *IEEE J. Sel. Top. Quantum Electron*. **2011**, 17, 333-346.
3. Miller, D.A.B. Device requirements for optical interconnects to Silicon chips. *Proceeding of the IEEE* **2009,** 97, 1166-1185.
4. Zheng, X.Z.; Chang, E.; Shubin, I.; Li, G.L.; Luo, Y.; Yao, J.; Thacker, H.; Lee, J.H.; Lexau, J.; Liu, F.; Amberg, P.; Raj, K.; Ho, R.; Cunningham, J.E.; Krishnamoorthy, A.V. A 33mW 100Gbps CMOS Silicon photonic WDM transmitter using off-chip laser sources. *Optical Fiber Communication Conf. and Exposition and the National Fiber Optic Engineers Conf.,* Anaheim, California, USA, March 17-21, **2013**, PDP5C-9.
5. Maier, S.A. *Plasmonics: Fundamentals and Applications*; Springer Publishing: New York, 2007.
6. Hill, M.T.; Marell, M.; Leong, E.S.P.; Smalbrugge, B.; Zhu, Y.; Sun, M.; van Veldhoven, P.J.;

Geluk, E.J.; Karouta, F.; Oei, Y.S.; Nötzel, R.; Ning, C.Z.; Smit, M.K. Lasing in metal-insulator-metal sub-wavelength plasmonic waveguides. *Opt. Express* **2009**, 17, 11107-11112.

7. Noginov, M.A.; Zhu, G.; Belgrave, A.M.; Bakker, R.; Shalaev, V.M.; Narimanov, E.E.; Stout, S.; Herz, E.; Suteewong, T.; Wiesner, U. Demonstration of a spaser-based nanolaser. *Nature* **2009**, 460, 1110-1112.
8. Sorger, V.J.; Zhang, X. Spotlight on Plasmon Lasers. *Science* **2011**, 333, 709-710.
9. Oulton, R.F.; Sorger, V.J.; Zentgraf, T.; Ma, R.M.; Gladden, C.; Dai, L.; Bartal, G.; Zhang, X. Plasmon lasers at deep subwavelength scale. *Nature* **2009**, 461, 629-632.
10. Yu, K.; Lakhani, A.; Wu, M.C. Subwavelength metal-optic semiconductor nanopatch lasers. *Opt. Express* **2010**, 18, 8790-8799.
11. Ma, R.M.; Oulton, R.F.; Sorger, V.J.; Bartal, G.; Zhang X. Room-temperature sub-diffraction-limited plasmon laser by total internal reflection. *Nat. Mater*. **2011**, 10, 110-113.
12. Ma, R.M.; Yin, X.B.; Oulton, R.F. Sorger, V.J.; Zhang, X. Multiplexed and electrically modulated plasmon laser circuit. *Nano Lett*. **2012**, 12, 5396-5402.
13. Nezhad, M.P.; Simic, A.; Bondarenko, Q.; Slutsky, B.; Mizrahi, A.; Feng, L.; Lomakin, V.; Fainman, Y. Room-temperature subwavelength metallo-dielectric lasers. *Nat. Photon*. **2010**, 4, 395-399.
14. Ding, K.; Hill, M.T.; Liu, Z.C.; Yin, L.J.; van Veldhoven, P.J.; Ning, C.Z. Record performance of electrical injection sub-wavelength metallic-cavity semiconductor lasers at room temperature. *Opt. Express* **2013**, 21, 4728-4733.
15. Hill, M.T.; Oei, Y.S.; Smalbrugge, B.; Zhu, Y.; de Vries, T.; van Veldhoven, P.J.; van Otten, F.W. M.; Eijkemans, T.J.; Turkiewicz, J.P.; de Waardt, H.; Geluk, E.J.; Kwon, S.H.; Lee, Y.H.; Nötzel, R.; Smit, M.K. Lasing in metallic-coated nanocavities. *Nat. Photon*. **2007**, 1, 589-594.
16. Khajavikhan, M.; Simic, A.; Katz, M.; Lee, J.H.; Slutsky, B.; Mizrahi, A.; Lomakin, V.; Fainman, Y. Thresholdless nanoscale coaxial lasers. *Nature* **2012**, 482, 204-207.
17. Kwon, S.H.; Kang, J.H.; Seassal, C.; Kim, S.K.; Regreny, P.; Lee, Y.H.; Lieber, C.M.; Park, H.G. Subwavelength plasmonic lasing from a semiconductor nanodisk with silver nanopan cavity. *Nano Lett*. **2010**, 10, 3679-3683.
18. Lu, C.Y.; Chang, S.W.; Chuang, S.L.; Germann, T.D.; Bimberg, D. Metal-cavity surface-emitting microlaser at room temperature. *Appl. Phys. Lett.* **2010**, 96, 251101.
19. Chuang, S.L.; Bimberg, D. Metal-cavity nanolasers. *IEEE Photonics J*. **2011**, 3, 288-292.
20. Ding, K.; Ning, C.Z. Metallic subwavelength-cavity semiconductor nanolasers. *Light Sci. Appl*. **2012**, 1, e20.
21. Kim, M.K.; Li, Z.; Huang, K.; Going, R.; Wu, M.C.; Choo, H. Engineering of metal-clad optical nanocavity to optimize coupling with integrated waveguides. *Opt. Express* **2013**, 21, 25796-25804.
22. Bondarenko, O.; Simic, A.; Gu, Q.; Lee, J.H.; Slutsky, B.; Nezhad, M.P.; Fainman, Y. Wafer bonded subwavelength metallo-dielectric laser. *IEEE Photonics J*. **2011**, 3, 608-616.
23. Halioua, Y.; Bazin, A.; Monnier, P.; Karle, T.J.; Roelkens, G.; Sagnes, I.; Raj, R.; Raineri, F. Hybrid III-V semiconductor/silicon nanolaser. *Opt. Express* **2011**, 19, 9221-9231.
24. Huang, K.C.Y.; Seo, M.K.; Sarmiento, T.; Huo, Y.J.; Harris, J.S.; Brongersma, M.L. Electrically driven subwavelength optical nanocircuits. *Nat. Photon*. **2014**, 8, 244-249.

25. Purcell, E.M. Spontaneous emission probabilities at radio frequencies. *Phys. Rev.* **1946**, 69, 681.
26. Holmgaard, T.; Bozhevolnyi, S.I. Theoretical analysis of dielectric-loaded surface plasmon-polariton waveguides. *Phys. Rev. B* **2007**, 75, 245405.
27. Lakhani, A.M.; Yu, K.; Wu, M.C. Lasing in subwavelength semiconductor nanopatches. *Semicond. Sci. Technol*. **2011**, 26, 014013.
28. Huang, Z.L.; Wang, J.F.; Liu, Z.H.; Xu, G.Z.; Cao, B.; Wang, C.H.; Xu, K. Nanoscale active hybrid plasmonic laser with a metal-clad metal-insulator-semiconductor square resonator. *J. Opt. Soc. Am. B* **2014**, 31, 1422-1429.
29. Briggs R.M.; Grandidier, J.; Burgos, S.P.; Feigenbaum E.; Atwater. H.A. Efficient coupling between dielectric-loaded plasmonic and Silicon photonic waveguides. *Nano Lett*. **2010**, 10, 4851-4857.
30. Fan, P.Y.; Colombo, C.; Huang, K.C.Y.; Krogstrup, P.; Nygård, J.; Morral, A.F.I.; Brongersma, M.L. An electrically-driven GaAs nanowire surface plasmon source. *Nano Lett*. **2012**, 12, 4943-4947.
31. Cai, M.; Hunziker, G.; Vahala, K. Fiber-optic add-drop device based on a silica microsphere-whispering gallery mode system. *IEEE Photon. Technol. Lett*. **1999**, 11, 686-687.
32. Mikulics, M.; Zheng, X.; Adam, R.; Sobolewski, R.; Kordos, P. High-speed photoconductive switch based on low-temperature GaAs transferred on SiO_2-Si substrate. *IEEE Photon. Technol. Lett*. **2003**, 15, 528-530.
33. Ding, K.; Ning, C.Z. Fabrication challenges of electrical injection metallic cavity semiconductor nanolasers. *Semicond. Sci. Technol*. **2013**, 28, 124002.
34. Ma, R.M.; Oulton, R.F.; Sorger, V.J.; Zhang, X. Plasmon lasers: coherent light source at molecular scales. *Laser Photon. Rev*. **2013**, 7, 1-21.
35. Gu, Q.; Smalley, J.S.T.; Nezhad, M.P.; Simic, A.; Lee, J.H.; Katz, M.; Bondarenko, O.; Slutsky, B.; Mizrahi, A.; Lomakin, V.; Fainman, Y. Subwavelength semiconductor lasers for dense chip-scale integration. *Adv. Opt. Photonics* **2014**, 6, 1-56.
36. Passlack, M.; Hong, M.; Opila, R.L.; Mannaerts, J.P.; Kwo, J.R. GaAs surface passivation using in-situ oxide deposition. *Appl. Surf. Sci*. **1996**, 104-105, 441-447.
37. Chuang, S.L. *Physics of Optoelectronic Devices*; Wiley: New York, 1995.
38. Lu, C.Y.; Ni, C.Y.; Zhang, M.; Chuang, S.L.; Bimberg, D.H. Metal-cavity surface-emitting microlasers with size reduction: theory and experiment. *IEEE J. Sel. Top. Quantum Electron*. **2013**, 19, 1701809.
39. Sarkisyan, T.V.; Oraevsky, A.N.; Rosenberger, A.T.; Rolleigh, R.L.; Bandy, D.K. Nonlinear gain and carrier temperature dynamics in semiconductor laser media. *J. Opt. Soc. Am. B* **1998**, 15, 1107-1119.
40. Genov, D.A.; Oulton, R.F.; Bartal, G.; Zhang, X. Anomalous spectral scaling of light emission rates in low-dimensional metallic nanostructures. *Phy. Rev. B* **2011**, 83, 245312.
41. Gu, Q.; Smalley, J.S.T.; Shane, J.; Bondarenko, O.; Fainman, Y. Temperature effects in metal-clad semiconductor nanolasers. *Nanophotonics* **2015**, 4, 1-18.
42. Miller, D.A.B. Energy consumption in optical modulators for interconnects. *Opt. Express* **2012**, 20, A293-A308.
43. Sorger, V.J. Nano-optics gets practical Plasmon Modulators. *Nat. Nanotechnol*. **2015**, 10, 11-15.

44. Wahl, P.; Tanemura, T.; Debaes, C.; Vermeulen, N.; Van Erps, J.; Miller, D.A.B.; Thienpont, H. Energy-per-bit limits in plasmonic integrated photodetectors. *IEEE J. Sel. Top. Quantum Electron*. **2013**, 19, 3800210b.
45. Adachi, S. Optical properties of $Al_xGa_{1-x}As$ alloys. *Phys. Rev. B* **1988**, 38, 12345-12352.
46. Lin, C.H.; Meese, J.M.; Wroge, M.L.; Weng, C.J. Effect of GaAs/AlGaAs quantum-well structure on refractive index. *IEEE Photon. Technol. Lett*. **1994**, 6, 623-625.
47. FDTD Solutions software by Lumerical Solutions, Inc. http://docs.lumerical.com.

TABLES

Table 1. Parametric source scaling and PIC device road mapping defining three technological regimes. Assuming typical regime-dependent device footprints define a capacitive-limited intrinsic device efficiency (assumptions: ε_r = 10, capacitive distance = 10 nm, bias voltage = 1.5 V), and a required number of photons per bit given for a given operating wavelength (λ = 1.55 μm). The capacitive modulation bandwidth (in gigabits per second = Gbps, assuming on-off-keying) is inverse proportional to the electrical capacitance (i.e. $f_{3dB\text{-}BW} \sim 1/RC$, R = resistance, C = capacitance). Diffraction limited 'classical' devices have prohibitively high power consumption and limit integration to tens of devices on-chip, however requiring no LMI enhancement factor (Q/V_n). The next technological steps are nanoscale devices, can not only be more compact, but are also more power efficient, thus allowing for higher integration, yet require moderate LMI enhancement. Quantum devices, while potentially very efficient and fast, require demanding LMI enhancements. [a)] Q-factors top to bottom: 10^4, 10^2, and 1.

Regime	**Footprint** (μm^2)	**Efficiency** (~J/bit)	**Photons per bit**	**Data Rate** (Gbps) **10**	**100**	**1000**	**Required** [a)] Q/V_n
Classical	100	1p	10^7	0.01	0.1	1	none
Nano	0.25	1f	10^4	0.01m	0.1m	1m	$<10^2$
Quantum	10^{-4}	1a	10	0.01μ	0.1μ	1μ	$>10^4$
				Average Power (W)			